Draft version January 5, 2022
Preprint typeset using LaTeX style emulateapj v. 12/16/11

arXiv:2102.11295v1 [astro-ph.HE] 22 Feb 2021

GRB 191016A: A LONG GAMMA-RAY BURST DETECTED BY TESS

Krista Lynne Smith[1,2,3], Ryan Ridden-Harper[4], Michael Fausnaugh[5], Tansu Daylan[5], Nicola Omodei[6], Judith Racusin[7], Zachary Weaver[8], Thomas Barclay[9,10], Péter Veres[11], D. Alexander Kann[12], and Makoto Arimoto[13]

Draft version January 5, 2022

ABSTRACT

The TESS exoplanet-hunting mission detected the rising and decaying optical afterglow of GRB 191016A, a long Gamma-Ray Burst (GRB) detected by *Swift*-BAT but without prompt XRT or UVOT follow-up due to proximity to the moon. The afterglow has a late peak at least 1000 seconds after the BAT trigger, with a brightest-detected TESS datapoint at 2589.7 s post-trigger. The burst was not detected by *Fermi*-LAT, but was detected by *Fermi*-GBM without triggering, possibly due to the gradual nature of rising light curve. Using ground-based photometry, we estimate a photometric redshift of $z_{\rm phot} = 3.29 \pm 0.40$. Combined with the high-energy emission and optical peak time derived from TESS, estimates of the bulk Lorentz factor $\Gamma_{\rm BL}$ range from $90 - 133$. The burst is relatively bright, with a peak optical magnitude in ground-based follow-up of $R = 15.1$ mag. Using published distributions of GRB afterglows and considering the TESS sensitivity and sampling, we estimate that TESS is likely to detect ~ 1 GRB afterglow per year above its magnitude limit.

Keywords: galaxies:active - galaxies:nuclei - galaxies:Seyfert - radio:galaxies - stars:formation

1. INTRODUCTION

The Transiting Exoplanet Survey Satellite, or TESS (Ricker et al. 2015), is currently in the midst of a nearly all-sky timing survey in search of transiting planets around M-dwarfs. On 2019 October 16 the Burst Alert Telescope (BAT; Barthelmy et al. 2005) onboard the *Neil Gehrels Swift Observatory* (Gehrels et al. 2004, *Swift* hereafter) detected a gamma ray burst (GRB) in the portion of the sky being monitored by TESS (Gropp et al. 2019). The burst occurred too close to the moon for *Swift* to safely slew to its position, preventing UVOT and XRT follow-up until over 11 hours after the BAT trigger. The TESS data are therefore the only space-based follow-up for the burst before this time. Several ground-based observatories detected the counterpart and afterglow simultaneously with the TESS measurements, as documented in the GRB Coordinates Network (GCN)[14](Watson et al. 2019a,b; Zheng et al. 2019; Hu et al. 2019; Kim et al. 2019; Schady & Bolmer 2019; Toma et al. 2019).

TESS clearly detects the rising pre-peak light curve of this long GRB. Here, we present the TESS light curve and discuss the viability of TESS data to help constrain properties of GRBs that happen to occur within its field of view.

In Section 2, we give the parameters of the burst as reported by *Swift*. In Section 3 we discuss the TESS mission and the extraction of the light curve. Section 4 discusses the high energy emission from the burst as observed by *Fermi*, while Section 5 presents the optical afterglow properties and how they compare to known bursts. Section 6 presents the photometric modelling to determine the redshift of the afterglow. In Section 7, we use the redshift and burst parameters to calculate the bulk Lorentz factor. Section 8 presents the calculation of how many bursts may be observable with TESS, and Section 9 provides a brief conclusive summary.

When redshift is dealt with in this document, we have assumed a cosmology with $H_0 = 69.6$ km s^{-1} Mpc^{-1}, $\Omega_M = 0.286$, and $\Omega_\Lambda = 0.714$.

2. GRB 191016A

The BAT trigger for GRB 191016A occurred at 04:09:00.91 UT on 2019 October 16. The enhanced position was reported as RA=02:01:04.67, DEC=+24:30:35.3 (J2000), corresponding to no cataloged galaxy. The BAT light curve lasts for approximately 210 seconds after the trigger, with a poorly-constrained T_{90} duration of 220±180 s. The burst had a fluence of 1.12×10^{-5} erg cm^{-2} in the energy range $15 - 350$ keV regardless of whether the light curve is modelled as a power law with or without a cutoff; in both models the best fitting power law photon index is $\Gamma_{\rm ph} = 1.54 \pm 0.09$,

[1] KIPAC at SLAC, Stanford University, Menlo Park, CA 94025, USA; klynne@stanford.edu
[2] Einstein Fellow
[3] Southern Methodist University, Department of Physics, Dallas, TX 75205, USA
[4] Research School of Astronomy & Astrophysics, Mount Stromlo Observatory, The Australian National University, Cotter Road, Weston Creek, ACT 2611, Australia
[5] MIT Kavli Institute for Astrophysics and Space Research, Massachusetts Institute of Technology, Cambridge, MA, USA
[6] W. W. Hansen Experimental Physics Laboratory, Kavli Institute for Particle Astrophysics and Cosmology, Department of Physics and SLAC National Accelerator Laboratory, Stanford University, Stanford, CA 94305, USA
[7] Astrophysics Science Division, NASA Goddard Space Flight Center, Mail Code 661, Greenbelt, MD 20771, USA
[8] Institute for Astrophysical Research, Boston University, 725 Commonwealth Avenue, Boston, MA, 02215 USA
[9] Exoplanets and Stellar Astrophysics Laboratory, Code 667, NASA Goddard Space Flight Center, Greenbelt, MD 20771, USA
[10] University of Maryland, Baltimore County, 1000 Hilltop Circle, Baltimore, MD 21250, USA
[11] Center for Space Plasma and Aeronomic Research, University of Alabama in Huntsville, Huntsville, AL 35899, USA
[12] Instituto de Astrofísica de Andalucía (IAA-CSIC), Glorieta de la Astronomía s/n, 18008 Granada, Spain
[13] Faculty of Mathematics and Physics, Institute of Science and Engineering, Kanazawa University, Kakuma, Kanazawa, Ishikawa 920-1192, Japan

[14] https://gcn.gsfc.nasa.gov/

where the sign convention used is $E^{-\Gamma_{\rm ph}}$.

Due to the moon constraints of the *Swift*-XRT and UVOT telescopes, the satellite did not immediately slew to the position of the burst. This means that the XRT and UVOT light curves of the afterglow, typically simultaneous with ground-based follow-up, are delayed by several hours. GRB 191016A was at 72° from the *Fermi*-Large Area Telescope (LAT, Atwood et al. 2009) boresight. The burst entered the *Fermi*-LAT field of view about 4 ks after the *Swift*-BAT trigger, but was not detected by LAT. Despite being in the field-of-view of the *Fermi* Gamma-ray Burst Monitor (GBM, Meegan et al. 2009), it did not cause a trigger but was detected; see Section 4 for details.

The earliest follow-up of the burst was ground-based, beginning a few hundred seconds after the trigger, as chronicled in the GCN (for references, see the Introduction); the burst peaks at an apparent magnitude of $R = 15.1$ mag.

3. THE TESS MISSION AND LIGHT CURVE

During the recently completed TESS primary mission phase, the spacecraft observed each 24×96 degree sector of the sky (over 2300 square degrees) continuously for 27 days, recording integrations every 30-minutes, before moving on to the next sector. At high ecliptic latitudes, the sectors overlap, resulting in light curves with extended durations. The bandpass is wide and monolithic, spanning the red-optical to the NIR ($\sim 600 - 1050$ nm). GRB 191016A occurred during Sector 17, in a low ecliptic latitude corresponding to the minimum ∼27-day baseline. The photometric precision of the light curves are 0.1-1% at 15-16th magnitude, the peak brightness of this burst. With the start of the TESS extended mission on July 5, 2020, TESS has increased its monitoring cadence from 30 minutes to 10 minutes.

TESS does not release reduced light curves for all regions of the sky. Instead, the mission releases the full-frame images (FFIs) for each cadence in a sector, and requires observers to perform their own photometric extraction, background subtraction and systematic error corrections. The optimal way to do this can differ based on the position on the detector, crowdedness of the source region, the magnitude of the source, and nature of the variability being studied (see, for example, the challenges in adapting the *Kepler* light curves for use on extragalactic targets; Smith 2019).

The TESS satellite is optimized to efficiently search for exoplanet transit signals around more than 20,000 stars simultaneously. This mission is not designed for deep, high resolution studies of individual objects. The TESS angular resolution is extremely low, with pixels measuring 21″ across, frequently resulting in a situation where no photometric extraction aperture is possible that does not include incidental nearby sources. Extraction of the light curve is thus dependent upon the source properties desired, the sky environment of the source, and the location on the TESS detector. To ensure that any conclusions we draw in our analysis are robust against different methods, we extract the light curve in three different ways, described in this section.

3.1. *Light Curve Extractions: Simple Background Subtraction*

In this simplest method of systematics mitigation, we begin by requesting a cutout of the sky around the region of interest using the online TESSCut tool[15] (Brasseur et al. 2019); this produces a FITS file with photometric images at every cadence during the monitored sector(s), with all of the information provided in the full FFIs (e.g., quality flags and time/flux errors). The bulk of the manipulation of the FITS files is accomplished with the AstroPy library (Astropy Collaboration et al. 2013, 2018). We then choose an extraction aperture, by eye, to maximize the flux from the GRB afterglow while still avoiding nearby sources, as well as a nearby background region devoid of sources with the same pixel size as the extraction aperture. We perform aperture photometry from each cadence that is not flagged for pointing instability by the TESS mission, from both the extraction and background apertures. Finally, the background light curve is subtracted from the source light curve. The chosen source and background apertures and the resulting light curve are shown in the first row of Figure 1. Note that Figure 1 shows the light curves in TESS instrumental units, as is usual for TESS photometric studies. There is currently no accepted method of converting TESS counts to a magnitude system. The light curve is presented again, in a context comparative to other afterglows, in Section 5, in more traditional units for GRBs, with an attempt at a magnitude conversion.

3.2. *Light Curve Extraction: Interpolated Background*

For this method, we interpolate the TESS background from sky pixels. We also utilise TESSCut (Brasseur et al. 2019) in conjunction with the Kepler/TESS reduction packages from Lightkurve (Lightkurve Collaboration et al. 2018) for this method, to get a 50×50 pixel TESS image of the region surrounding the GRB. To identify which pixels are background pixels we simulate a 50×50 pixel TESS image, centered on the GRB, using the Gaia source catalogue (Gaia Collaboration et al. 2018). The Gaia sources are mapped onto the simulated image with the TESS WCS. We convert Gaia source magnitudes to TESS magnitudes via $m_{TESS} = m_{Gaia} - 0.5$ (Stassun et al. 2018), and the subsequent TESS magnitudes to counts, with a zeropoint of 20.44. We then convolve the Gaia sources with a model TESS PSF, using methodology based on the *DAVE* pipeline (Kostov et al. 2019). Finally, all pixels of the simulated image with counts less than a limit are selected as background pixels. We interpolate the background signal from the background pixels to all pixels in the image. This method of simulating the image allows for a clear determination of which pixels are dominated by the background.

Following background subtraction simple aperture photometry is performed with a 2×2 pixel aperture. The resulting light curve is shown in in the middle panel of Figure 1.

3.3. *Light Curve Extraction: PSF-Fitting*

Modeling the target flux via PSF yields an alternative method to extract the flux of the target in each time bin. Towards this purpose, we perform PSF photometry of the target given the TESS full frame image data. We employ

[15] https://mast.stsci.edu/tesscut/

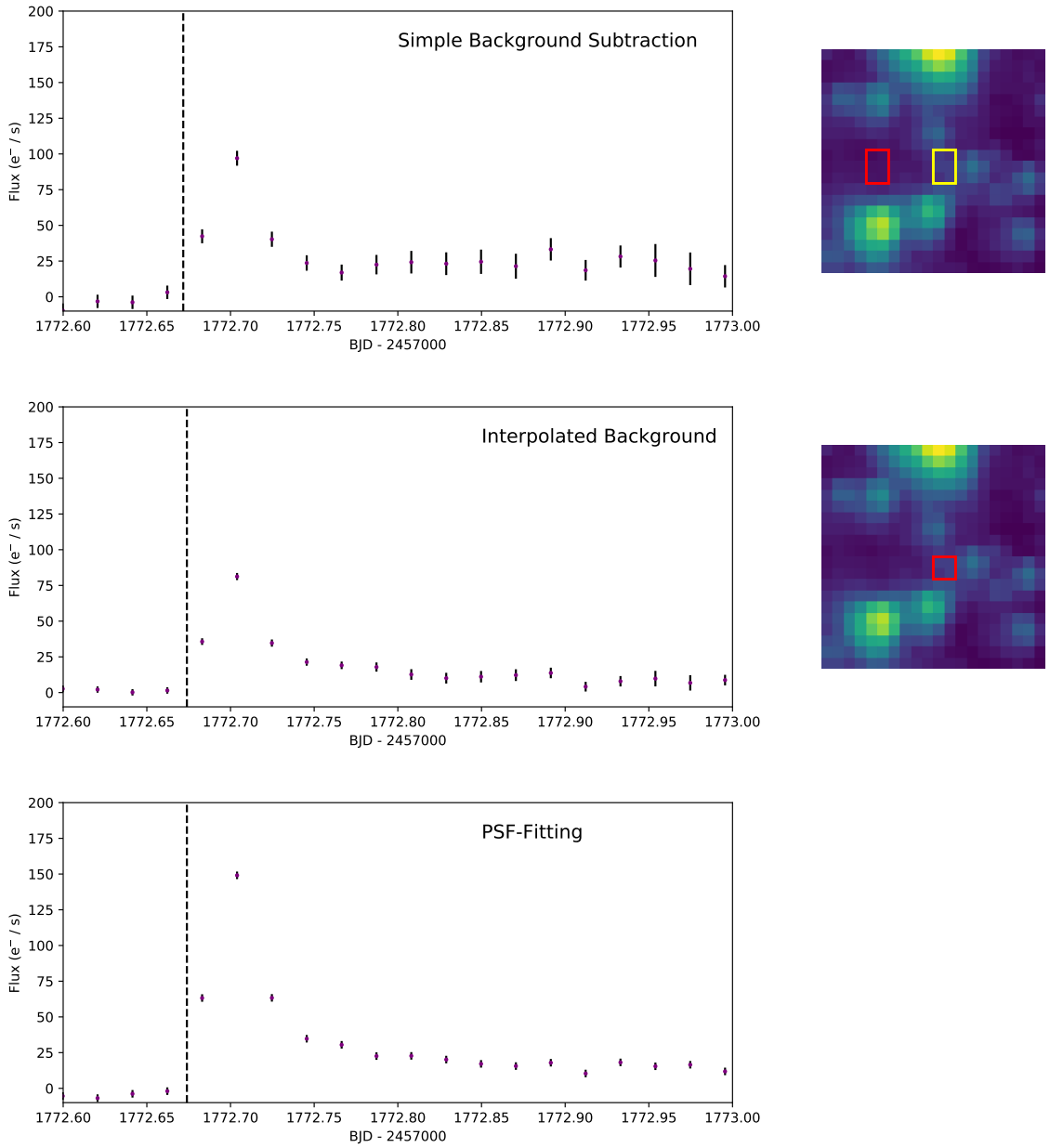

Figure 1. Light curves (left) and extraction and background apertures (right) of GRB 191016A. The first row shows the light curve reduced with simple background subtraction as derived in Section 3.1, the second row shows the light curve derived using the interpolated background estimation method described in Section 3.2, and the third row shows the light curve derived using the PSF-fitting method described in Section 3.3 (because the PSF is fitted at each cadence, no stable aperture exists). All light curves are normalized by subtracting the median of the first 100 cadences of the sector (not plotted), well before the *Swift* trigger, which is denoted by the vertical dashed lines.

the Pixel Response Function (PRF) model constructed by the TESS mission. This takes into account the optical PSF as well as the pointing jitter of the detector. We then use 13×13 pixel PRF models that are upsampled by a factor 9. We interpolate the model up to the third order in subpixel shifts and evaluate the model images of the target and nearby known point sources in the TESS Input Catalog (TIC, Stassun et al. 2018). Finally, using these point source models as templates, we perform linear regression to infer the fluxes of all sources in each time bin. Inclusion of the templates of the nearby sources enables marginalization over the neighbors and reduces potential flux contamination from nearby sources.

Each light curve and extraction aperture is plotted in Figure 1. The light curve is clearly rising in the first data point following the BAT trigger, peaks at the subsequent point, and then declines. The afterglow falls below the TESS limiting magnitude as the light curve flattens out; note that the post-burst baseline may be higher than the pre-burst baseline due to an increase in the lunar scattered light. After the TESS limit is reached, ground-based follow-up is needed to explore the afterglow evolution at fainter magnitudes than $V \sim 18$ mag. In Figure 2, we show the sky image from TESS in the cadence before the BAT trigger and at the TESS peak cadence, with contrast enhanced for easier visibility. The extrac-

tion aperture shown in Figure 1 encompasses the new afterglow source PSF as completely as possible without including the nearby targets.

4. HIGH ENERGY EMISSION

In this section we discuss the gamma ray emission from GRB 191016A. Although undetected by *Fermi*-LAT, the burst was detected by both *Swift*-BAT (the trigger) and *Fermi*-GBM (no trigger). The BAT light curve is shown in Figure 3, obtained from the *Swift* Burst Analyser[16] (Evans et al. 2010) with a S/N = 5 binning. The GBM light curve is shown in Figure 4.

High-energy emission from GRBs has been observed by *Fermi*-LAT up to >10 ks post-trigger (Ajello et al. 2019). We preform an unbinned likelihood analysis in the time window between 3.9 ks and 5.4 ks, when the GRB was in the LAT FoV, in the energy range of 0.1 − 1 GeV. The GRB spectrum is described with a simple power law, and the contribution of the galactic and extragalactic diffuse emissions are added to the model. We select events within a Region Of Interest (ROI) of 12 degrees from the GRB localization. The time interval is selected by requiring that the entire ROI is visible, with a zenith angle <100 degrees. No significant emission at high energy is detected. We compute a flux upper limit of 1.6×10^{-6} photon cm^{-2} s^{-1}, corresponding to an energy flux upper limit of 1.2×10^{-9} erg cm^{-2} s^{-1} assuming a photon index of $\Gamma_{\rm ph} = 2$, typical of LAT GRBs.

Even though GRB 191016A was in its field of view, Fermi-GBM was not triggered. The GBM `targeted search` (Goldstein et al. 2019) is the most sensitive, coherent search for GRB-like signals. During the automatic processing of external triggers in the GBM continuous data, the `targeted search` found a significant signal consistent in time, sky location and lightcurve morphology with GRB 191016A. The reason GRB 191016A did not trigger GBM is likely an interplay between different effects: (1) a gradual rise in intensity for this burst (2) the timescale on which GBM calculates the background rates to determine excess (3) variations in the gamma-ray background at the time of GRB 191016A due to the routine slewing of the spacecraft.

We performed standard spectral analysis using `RMfit`[17]. We selected data from $T_0-31.7$ s to $T_0+58.5$ s relative to the Swift trigger time. The best fitting spectrum is a power law with an exponential cutoff ($dN/dE \propto E^{-\Gamma_{\rm ph}} \exp(-E(2-\Gamma_{\rm ph})/E_{\rm peak})$. The photon index $\Gamma_{\rm ph} = 1.16 \pm 0.07$ and the energy where the νF_ν spectrum peaks, $E_{\rm peak} = 197 \pm 22$ keV. The flux in this time interval is $F = (1.04\pm0.05)\times10^{-7}$ erg s^{-1} cm^{-2} (10-1000 keV range). Using the method described in Bloom et al. (2001), we integrate the spectrum in the canonical 1 keV -10 MeV range and perform the k-correction to obtain the isotropic-equivalent energy in gamma rays. We calculate $E_{\gamma,\rm iso} = (2.37 \pm 0.12) \times 10^{53}$ erg.

5. A LATE-PEAKING AFTERGLOW

The brightest point in the TESS light curve occurs at 2589.7 s after the BAT trigger. This is significantly later than a typical long GRB in which the optical rise is observed; Oates et al. (2009) find that in their sample of 27 UVOT afterglows, all light curves are decaying by 500 s after trigger in the observer's frame. Such a late peak is not unprecedented, however; peak times of $\sim 10^3$ seconds are still within the tail of the distributions reported by Ghirlanda et al. (2018) for 67 afterglows with observed peaks.

In Figure 5, we show the three TESS afterglow light curves as computed in Section 3 and the ground-based GCN light curve, overlaid upon the large sample of optical afterglows of long GRBs from Kann et al. (2010). Although the TESS light curves are relatively bright, neither their peak magnitudes nor late peaking time is far out of the ordinary. Kann et al. (2010) (their Figure 7) also show some examples of afterglows that peak at significantly later times, including GRB 970508 which peaked after one day.

A very important caveat is necessary when comparing the brightness of the TESS afterglow to others in the plot, however: there is currently no accepted conversion from TESS counts (as shown in Figure 1) and any conventional magnitude system. This is primarily due to the monolithic and unusual TESS bandpass. In order to make a reasonable approximation, we have used the statement in the TESS Instrument Handbook[18] that 15,000 e$^-$s^{-1} are generated by the cameras for a star of apparent magnitude $m = 10$. We have thereby calculated the "zero flux" of the TESS bandpass to be $\sim 1.5\times10^8$ e$^-$ s^{-1}, via $m = -2.5\log(F/F_0)$. This number is roughly consistent with what is obtained by comparing the TESS light curves to the ground-based light curves, although the points are not simultaneous. Due to the roughness of this approach, the vertical normalization of the light curves on Figure 5 should be assumed to have large uncertainties.

Each of the TESS light curves yields a different temporal decay index α, where $F \propto t^\alpha$: $\alpha = -0.3$ for Simple Background Subtraction, $\alpha = -1.1$ for PSF Fitting, and $\alpha = -1.0$ for the Interpolated Background method. Since the Simple Background Subtraction method is most likely to suffer from contamination at later times, due to a large extraction aperture and no background modeling, its shallower index is not surprising. The decay index from the ground-based data is -1.4. These are all within the typical values for optical afterglows, as can be seen in Figure 5. In comparison to the optical afterglow decay indices of a sample of 139 long GRBs by Del Vecchio et al. (2016), the value for simple background subtraction, -0.3, is in the very shallow end, but the other values are among the most commonly found.

Some individual objects have been observed with late-peaking afterglows, typically following a long plateau phase in the optical and X-ray light curves. We do not have X-ray data during the optical rise time, since XRT did not slew to the position in time (Section 2), so we do not know whether the X-ray flux was consistent with this plateau behavior. There is only a single TESS data point between the trigger time and the apparent peak, which occurs 786 s after the trigger; already quite late compared to the Oates et al. (2009) sample. It is possible that this point occurs during an optical plateau,

[16] https://www.swift.ac.uk/burst_analyser/00929744/

[17] https://fermi.gsfc.nasa.gov/ssc/data/analysis/rmfit/

[18] https://heasarc.gsfc.nasa.gov/docs/tess/documentation.html

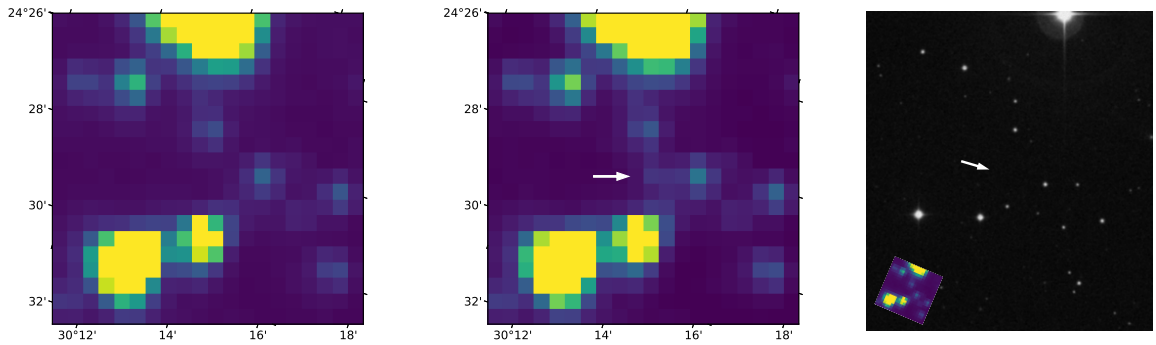

Figure 2. TESS full-frame image in the cadence just before the BAT trigger (left) and at the peak flux of the burst (center). The emergence of the afterglow is apparent in the center of the image, indicated by the white arrow. Contrast has been increased versus the right panel of Figure 1 in order to increase visibility. The right panel shows the same region of the sky, with a slightly different orientation, in the Digitized Sky Survey (DSS); a small inset of the TESS image is provided in the bottom left corner to demonstrate the change in orientation.

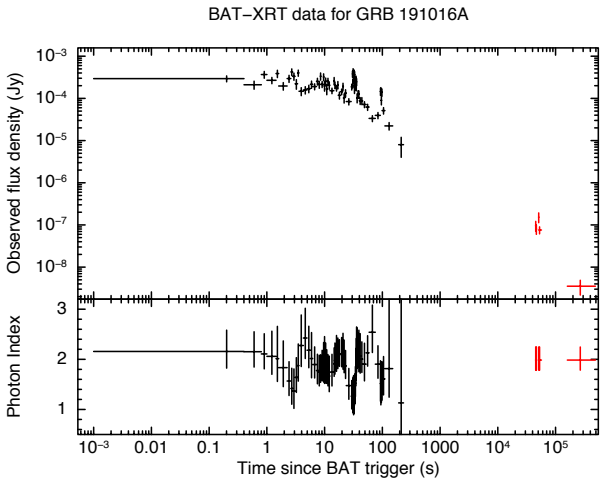

Figure 3. The *Swift*-BAT (black) and XRT (red) light curve for GRB 191016A, binned for S/N = 5. The evolution of the photon index is shown in the lower panel. This figure was obtained from the *Swift* Burst Analyser (Evans et al. 2010).

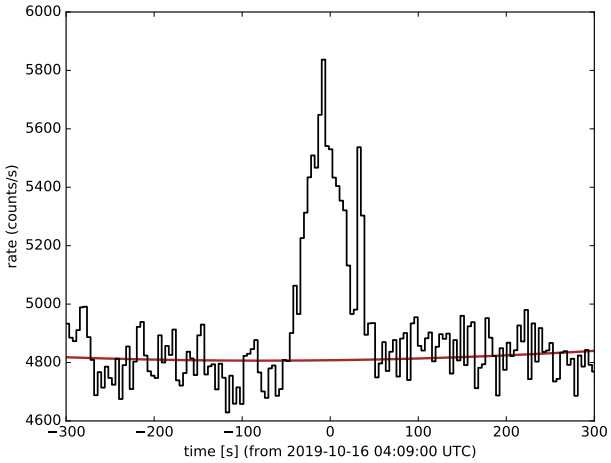

Figure 4. The summed *Fermi*-GBM lightcurve from NaI detectors 7, 9, a and b. The energy range is 50 − 300 keV and the temporal resolution is 4 s. The brown curve is the fitted polynomial background.

after which the flux rises rapidly to the peak data point before steeply decaying; the ground-based light curves do not indicate such a flattening, but do not definitively rule it out, either. If this is the case, it resembles the UVOT light curve of GRB 100418A, which peaked very late at approximately 50ks post-trigger, and was determined to most likely arise from continuous injection of energy into the forward shock (Marshall et al. 2011), as was the optical afterglow of GRB 060729 (Grupe et al. 2007). Indeed, a recent re-analysis of GRB 100418A by de Ugarte Postigo et al. (2018) showed that the afterglow re-brightened rapidly during the first day after the trigger, beginning 2.4 h after the burst. Other late-peaking afterglows have been interpreted as due to an off-axis viewing angle, where the peak occurs once the beam has widened sufficiently to include the line of sight, as in GRB 080710 ($t_{\rm peak} \sim 2 \times 10^3$ s, Krühler et al. 2009) and GRB 081028 ($t_{\rm peak} \sim 3 \times 10^4$ s, Margutti et al. 2010). The lack of a detection of GRB 191016A by *Fermi*-LAT may also support the off-axis interpretation for this burst; however, if the photometric redshift calculated below (Section 6), $z_{\rm phot} = 3.29$, is correct, a nondetection is perhaps to be expected, since only one GRB at a higher redshift has been detected by *Fermi*-LAT (GRB 080916C at $z = 4.35$, Abdo et al. 2009).

Late-peaking or complex afterglows can also be the result of a number of other physical scenarios, including reverse or forward shocks due to interaction with the ISM or progenitor winds (Sari & Piran 1999; Kobayashi et al. 2004), the peak frequency of the synchrotron emission moving through the observing band (Sari et al. 1998), or destruction of surrounding dust by radiation as the burst proceeds (Fruchter et al. 2001); see Oates et al. (2009) for a nice summary of these effects in greater detail.

6. ESTIMATING THE REDSHIFT

The only constraint placed on the redshift by the Gamma-ray Coordinates Network (GCN) circulars was $z < 4$, established by the RATIR team (Watson et al. 2019a).

In order to determine a more precise redshift, we make use of the GCN-reported GROND photometry (Schady & Bolmer 2019), plotted in Figure 6. Since we lack

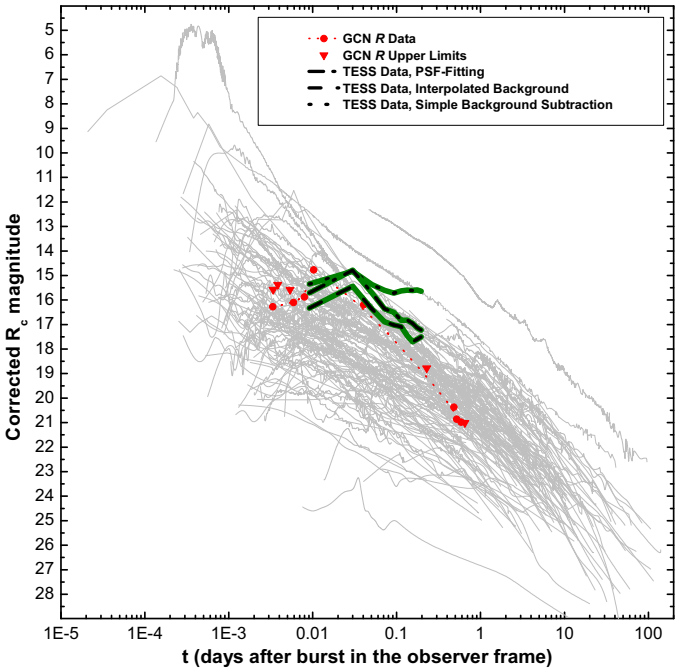

Figure 5. Optical afterglows of GRB 191016A from the three TESS approaches (Section 3; c.f. Figure 1), shown in green, compared to the long GRB afterglow sample from Kann et al. (2010). Also shown is the ground-based R-band light curve from the GCN, in red.

UVOT photometry, we do not have the fullest SED possible to constrain the redshift. However, with a simple model, we can arrive at a much more precise estimate than from the $g-r$ color alone.

We follow the prescription laid out in Krühler et al. (2011), which we describe briefly here, along with our simplifications. We begin by assuming that the intrinsic shape of the SED is a power law: $F_\nu(\lambda) = F_0\lambda^{\beta_0}$, where F_0 is a normalization constant. This intrinsic power law is then modified by extinction in the host galaxy, and by any neutral hydrogen in the intergalactic medium along the line of sight. Many GRB afterglows exhibit damped Lyman-α (DLA) absorption associated with the host galaxy, which must also be accounted for. The effect of extinction from within the Milky Way is negligible: $N_{HI,MW} = 7.57 \times 10^{20}$ cm^{-2} (HI4PI Collaboration et al. 2016). After these effects are accounted for, the observed spectrum can be modelled as

$$F_\nu(\lambda) = D_\alpha(z)F_0\lambda^{\beta_0}\exp[-\tau_{\rm dust}(z, A_V) - \tau_{\rm DLA}(z, N_H)]. \quad (1)$$

This model includes four free parameters: the redshift z, the intrinsic power law index β_0, the host galaxy extinction A_V, and the host column density of neutral hydrogen, N_H.

$D_\alpha(z)$ is the wavelength-averaged attenuation due to line blanketing from intergalactic neutral hydrogen. This is a monotonically-increasing function with redshift, which we model as in Madau (1995) (see their Figure 2). The first optical depth term, $\tau_{\rm dust}$, accounts for the host galaxy's own dust reddening. As described by Krühler et al. (2011), most bright GRB afterglows are well-modelled by a local reddening law (A_λ/A_V as a function of wavelength) based on the Small Magellanic Cloud, as opposed to models based on the Large Magellanic Cloud and the Milky Way; we nonetheless attempt the modelling using each of the three extinction laws, reproduced from Pei (1992); the lowest χ^2 values are found using the SMC version. With the reddening law in hand, we then follow Li et al. (2018): $\tau_{\rm dust} = (1/1.086)A_V\eta(\nu)$, where $\eta(\nu) = A_\lambda/A_V$.

The second optical depth term accounts for neutral hydrogen within the host galaxy ($\tau_{\rm DLA}$). This term is calculated following Totani et al. (2006): $\tau_{\rm DLA}(\lambda_{\rm obs}) = N_H\sigma_\alpha[\nu_{\rm obs}(1+z)]$, where $\nu_{\rm obs} = c/\lambda_{\rm obs}$, and σ_α is the exact formula for the frequency dependence of the Lyα cross-section (e.g., Madau & Rees 2000).

We fit Equation 1 to the SED, using the observed fluxes and mean wavelengths in each filter, with the definitions above using a Nelder-Mead minimization (Nelder & Mead 1965), allowing z, β, log N_H, and A_V to vary freely. We find that the best-fit model is achieved with $z_{\rm phot} = 3.29\pm0.40$, $\beta_0 = 0.16\pm0.02$, log $N_H = 23.0\pm0.97$, and log $A_V = -0.45 \pm 0.12$, which achieves a reduced $\chi^2 = 4.1$. The uncertainties in the fit parameters were estimated by using the results of the Nelder-Mead fit as the basis of a new least-squares fit, which generates a covariance matrix. The parameter errors are then the square root of the product of the diagonal of this matrix and the reduced chi-squared value of the least-squares fit.

These parameters are within observed distributions for GRB host galaxies as reported by Li et al. (2018). The value for N_H is quite high, but with a large uncertainty. Such values have been observed in other bursts, such as GRB 080607 ($z = 3.04$), and can be attributed either to molecular clouds along the line-of-sight in the host, or to the large-grained nature of dust at $z \sim 3$; see Corre et al. (2018) for a discussion.

The SED, GROND filters, and best-fitting model are shown in Figure 6, along with a few other models for comparison.

7. BULK LORENTZ FACTOR

If indeed one of the above scenarios causes the late-peaking afterglow and the the burst is on-axis, with a peak time corresponding to the start of the afterglow emission, one can derive the bulk Lorentz factor of the outflowing material using the equation and normalizations given by Molinari et al. (2007):

$$\Gamma_{\rm BL}(t_{\rm peak}) = \left[\frac{3E_\gamma(1+z)^3}{32\pi n m_{\rm p} c^5 \eta t_{\rm peak}^3}\right]^{1/8} \approx 160\left[\frac{E_{\gamma,53}(1+z)^3}{\eta_{0.2} n_0 t_{\rm peak,2}^3}\right]^{1/8}, \quad (2)$$

where $E_{\gamma,53}$ is the isoptropic-equivalent energy released in gamma rays normalized to 10^{53} erg, n_0 is the particle density of the surrounding medium in cm^{-3}, the normalized radiative efficiency $\eta_{0.2}$ is defined as $\eta = 0.2\eta_{0.2}$, and $t_{\rm peak,2} = t_{\rm peak}/(100{\rm s})$.

To calculate E_γ, the isotropic-equivalent energy released by the burst in gamma rays, we use the relation from Bloom et al. (2001):

$$E_{\rm iso} = S\frac{4\pi D_l^2}{1+z}k, \quad (3)$$

where S is the fluence, D_l is the luminosity distance and k is the cosmological k-correction factor, which is

approximately 2.5 at the best-fitting model redshift of $z_{\rm phot} = 3.29$. Using this and the fluence reported by the BAT detection (1.12×10^{-5} erg cm^{-2}; see Section 2), we find that $E_{\rm iso} = 6.61 \times 10^{53}$ erg. This is consistent with the most populous region of the observed range of $E_{\rm iso}$ found in a sample of 92 long GRBs by Ghirlanda et al. (2009). It is slightly higher than the value of $E_{\rm iso}$ found in Section 4; this inconsistency likely results from the longer observation time and smaller energy window for *Swift* ($15 - 350$ keV), and the fact that $E_{\rm peak}$ is not constrained by *Swift* observations. Extrapolating a power law from *Swift's* energy range to the 1 keV-10 MeV with no cutoff naturally results in a larger $E_{\rm iso}$. We therefore have two values of $E_{\rm iso}$ that can be used in Equation 2 for Lorentz factor calculation.

In addition to $E_{\rm iso}$, Equation 2 requires an estimate of $t_{\rm peak}$ to determine the bulk Lorentz factor $\Gamma_{\rm BL}$. We may either take the TESS peak at face-value and declare it the true peak time, or use extrapolation to determine the earliest possible peak time. The time between the BAT trigger and the brightest data point in the TESS light curve is 2589.7 seconds. Of course, the brightest TESS point may not represent the actual peak time, especially since the TESS cadence is a relatively coarse 30 minutes. The light curve is clearly still rising at the previous TESS data point, which occurs 786 s after the BAT trigger, providing a lower limit on $t_{\rm peak}$.

Based on the fact that the observed peak is relatively late, we may instead assume that the true peak occurred somewhere between the observed peak and the previous still-rising data point. Oates et al. (2009) calculated the best-fitting power law index to their sample of optical GRB afterglow light curves within the first 500 seconds, $\alpha_{<500}$. The steepest rising light curve in that sample had $\alpha_{<500} = 0.73 \pm 0.14$. If we use this value and extrapolate from the rising data point at $t = 786$s, and then see where that rising power law intersects with the declining power law between the observed peak and the following data point, the inferred peak time occurs at $t = 1316$s. Our two estimates for $t_{\rm peak}$ are therefore 2590s and 1316s.

If we take the observed peak cadence at $t = 2590$s to be the true peak and use the value of $E_{\rm iso}$ from Equation 3, the result is $\Gamma_{\rm BL} = 103$. This is consistent with the correlation between $\Gamma_{\rm BL}$ and $E_{\rm iso}$ for long GRBs from Ghirlanda et al. (2018) for a homogeneous ISM. Using the value of $E_{\rm iso}$ from Section 4, we obtain $\Gamma_{\rm BL} = 90$.

If we instead take the extrapolated peak time, $t = 1316s$, and use the value of $E_{\rm iso}$ from Equation 3, we obtain a Lorentz factor of $\Gamma_{\rm BL} = 133$. With $E_{\rm iso}$ from Section 4, we obtain $\Gamma_{\rm BL} = 117$.

These values of $\Gamma_{\rm BL}$ are consistent with the cumulative distribution of bulk Lorentz factors in afterglows with an observed $t_{\rm peak}$ for models that assume a homogeneous circumburst medium (Ghirlanda et al. 2018), except for $\Gamma_{\rm BL} = 90$, which is low compared to that distribution.

8. TESS AND GAMMA RAY BURSTS

In this section, we discuss how the TESS bandpass, sensitivity, sampling pattern and cadence will affect detection rates of GRBs, and to what extent a detection like GRB 191016A can be expected in the future.

The chief advantage TESS offers in studying optical afterglows of GRBs is its continuous coverage independent of a trigger, potentially capturing GRB afterglows

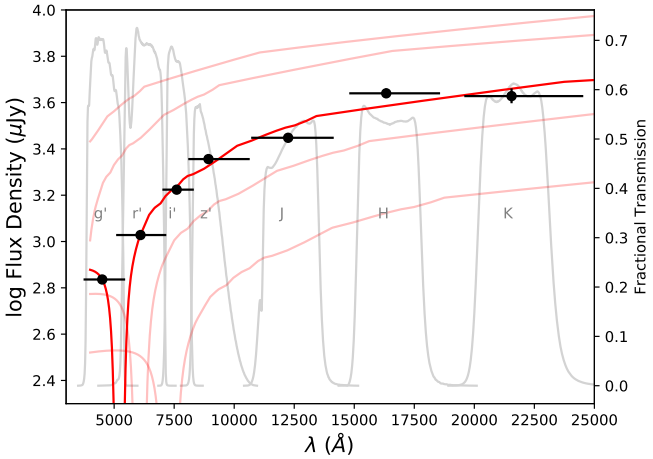

Figure 6. Spectral energy distribution from the GROND instrument at La Silla Observatory, the filter curves of which are shown. The best-fitting model corresponds to $z_{\rm phot} = 3.29$, and is shown in red. Other parameters are discussed in Section 6. Four other models are shown in pink, with identical parameters to the best-fitting model, but with redshifts 1, 2, 4, and 5 from top-left to bottom-right.

serendipitously, with a much higher sampling cadence than other timing surveys like the Zwicky Transient Facility (ZTF) or the Rubin Observatory's Legacy Survey of Space and Time (LSST). This is advantageous in the instance seen here, when observing constraints prevented a rapid slew by *Swift*, providing supplemental photometry to ground-based observations. It would be especially helpful in the case that a GRB does not trigger *Swift*-BAT, providing potentially the only optical follow-up in such cases; for example, for bursts which are only detected by *Fermi*-GBM.

A major limitation of TESS for GRB follow-up is its much brighter limiting magnitude compared to most ground-based telescopes. The TESS bandpass, as discussed in Section 3, is red-white monolithic, spanning 600-1100 nm. As such, it does not quite correspond to the traditional "white" filters on ground based telescopes. TESS uses a self-defined quantity, the "TESS magnitude," to determine its sensitivity limits, as can be seen in the TESS Instrument Handbook[19]. The photometric precision per 30-minute integration of the TESS cameras falls to $\sim 10\%$ at apparent magnitudes of ~ 18 mag (Ricker et al. 2015), and this is only true if a source is isolated and on a well-behaved portion of the CCD uncontaminated by scattered light.

With full frame images spaced every ten minutes, as will be the case starting in TESS Cycle 3, the worst-case scenario is that the burst occurs quasi-simultaneously with a TESS cadence. In this case, the next cadence will occur 10 minutes, or 600 seconds, later. This is after all of the light curves in the Oates et al. (2009) have passed their peak and begun to decay. The distribution of afterglow apparent magnitudes depends on the time after the burst and the morphological type of the light curve. Akerlof & Swan (2007) found that the distribution of afterglow apparent magnitudes of *Swift*-detected GRBs peaked at $R \sim 19.5$ mag. Wang et al. (2013) dif-

[19] https://heasarc.gsfc.nasa.gov/docs/tess/documentation.html

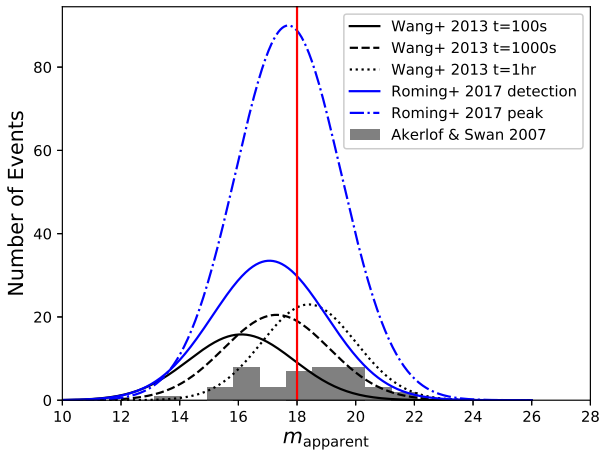

Figure 7. Histogram of apparent magnitudes, mostly in the R band but all in bands within the monolithic TESS filter. Blue curves correspond to the distributions reported by Roming et al. (2017); black curves correspond to the distributions reported by Wang et al. (2013); the grey histogram represents the distribution from Akerlof & Swan (2007). The TESS magnitude at which photometric precision falls below 10% is shown by the red vertical line.

ferentiated the observed afterglow population by post-burst time and light curve morphology, finding apparent magnitude distributions peaking at $R = 16.1$, 17.3, and 18.4 mag for 100 s, 1000 s, and 3600 s (1 hr) after the burst. Roming et al. (2017) report the UVOT magnitudes of the first-observed data point and the afterglow peak as 17.06 and 17.7 mag, respectively. We reproduce these populations in Figure 7, and overplot the TESS 10% photometry limit.

Based on these distributions, approximately 60% of bursts have afterglows that are above the TESS limiting magnitude for at least one cadence. This is a rough estimate, since the TESS bandpass does not correspond exactly to any of the bandpasses used in the works above. While it would be preferable to know how many bursts will have at least two cadences detected by TESS, precise calculations on this point are not useful, since 18 mag is not a hard limiting magnitude, and under good conditions, fainter objects can be detected by TESS and under poor conditions the limit is brighter.

In the case of GRB 191016A, the peak apparent magnitude is $R = 15.1$ mag, and we are able to detect one rising cadence, the peak cadence, and possibly 2 decaying cadences.

The most recent full catalog of UVOT GRB afterglows (Roming et al. 2017) contains 626 total bursts detected by multiple gamma ray missions over six years, of which 538 (86%) were followed up with UVOT. The majority of the remainder were too close to the sun or moon for follow-up, as is the case with GRB 191016A, while a few occurred during instrument downtime. Of the 538 bursts followed up by UVOT, 333 were detected in at least one of its filters. As can be seen in Figure 7, approximately 60% of these are brighter than 18th magnitude. Note that although these filters are ultraviolet through v, typical burst SEDs are brighter in the red/infrared, and so the probable detection fraction in the redder TESS bandpass is likely higher than 60%. Additionally, any influence of dust in the Milky Way, the host galaxy, and absorbers in the intergalactic medium are diminished at redder wavelengths. Spread over six years, this means that an occurrence rate of GRBs bright enough for TESS detection is about 33 per year. During a given sector, TESS is surveying approximately 2300 square degrees, or about 4% of the sky; thus, the likely rate of such a GRB occurring in the TESS field of view is 4% of 33, or about one per year. In order for TESS to observe it, it must remain above the limiting magnitude for long enough that the TESS 10-minute cadence will capture it. If we assume the very common temporal decay index $\alpha = -1.4$, a burst peaking at $m = 16$ mag will decay below $m = 18$ mag in 26s. Bursts peaking at $m = 15$ and 14 mag will decay below $m = 18$ mag in 138 and 720 seconds respectively; meaning that in the worst case scenario of a burst occurring just before a TESS cadence, only afterglows with relatively bright (< 14 mag) peaks will be captured. The range of temporal decay indices, however, assures us that approximately half of bursts will have flatter decays than this, remaining brighter for longer. Given the uncertainties in the true limits of TESS detection, along with the possibility of TESS capturing the burst near to its peak and the positive effects of the redder TESS bandpass, a detection rate of one GRB afterglow per year remains a reliable estimate, if perhaps slightly optimistic. It is consistent with the current detection rate.

This discussion is valid only for GRBs powerful enough to trigger *Swift*, since the comparison samples in Figure 7 are based on *Swift* triggers, and with sufficient positional accuracy to localize to a TESS source. It is possible that the TESS-GRB detection rate may be slightly higher, if, for example, orphan afterglows are taken into account.

9. CONCLUSION

We have analyzed the TESS light curve and ground-based photometry of GRB 191016A, a long GRB detected by *Swift*-BAT. The afterglow has a late peak that is at least 1000 seconds after the BAT trigger, with a brightest-detected TESS datapoint at 2589.7 s. Using photometric modelling, we have determined the redshift of the afterglow to be $z_{\rm phot} = 3.29 \pm 0.40$. The burst was not immediately observed by the XRT and UVOT due to its proximity to the moon, which is true of about 14% of *Swift* bursts; the serendipitous ongoing monitoring of TESS therefore provided prompt follow-up within a few minutes that otherwise would have been missed for this burst, supplementing triggered ground-based observations. Simple arithmetic arguments based on archival afterglow samples imply that TESS will likely detect ~ 1 GRB afterglow per year above its magnitude limit, not accounting for afterglows without *Swift* triggers.

Support for KLS was provided by the National Aeronautics and Space Administration through Einstein Postdoctoral Fellowship Award Number PF7-180168, issued by the Chandra X-ray Observatory Center, which is operated by the Smithsonian Astrophysical Observatory for and on behalf of the National Aeronautics Space Administration under contract NAS8-03060. P.V. acknowledges support from NASA grants 80NSSC19K0595 and NNM11AA01A. This paper includes data col-

lected by the TESS mission. DAK acknowledges support from Spanish National Research Project RTI2018-098104-J-I00 (GRBPhot). Z.R.W. acknowledges support through NASA grant 80NSSC19K1731. Funding for the TESS mission is provided by the NASA Explorer Program. This work has made use of data from the European Space Agency (ESA) mission *Gaia* (`https://www.cosmos.esa.int/gaia`), processed by the *Gaia* Data Processing and Analysis Consortium (DPAC, `https://www.cosmos.esa.int/web/gaia/dpac/consortium`). Funding for the DPAC has been provided by national institutions, in particular the institutions participating in the *Gaia* Multilateral Agreement.

The Fermi-LAT Collaboration acknowledges generous ongoing support from a number of agencies and institutes that have supported both the development and the operation of the LAT, as well as scientific data analysis. These include the National Aeronautics and Space Administration and the Department of Energy in the United States; the Commissariat à l'Energie Atomique and the Centre National de la Recherche Scientifique/Institut National de Physique Nucléaire et de Physique des Particules in France; the Agenzia Spaziale Italiana and the Istituto Nazionale di Fisica Nucleare in Italy; the Ministry of Education, Culture, Sports, Science and Technology (MEXT), High Energy Accelerator Research Organization (KEK), and Japan Aerospace Exploration Agency (JAXA) in Japan; and the K. A. Wallenberg Foundation, the Swedish Research Council, and the Swedish National Space Agency in Sweden.

This work made use of data supplied by the UK Swift Science Data Centre at the University of Leicester.

The Digitized Sky Survey was produced at the Space Telescope Science Institute under U.S. Government grant NAG W-2166. The images of these surveys are based on photographic data obtained using the Oschin Schmidt Telescope on Palomar Mountain and the UK Schmidt Telescope. The plates were processed into the present compressed digital form with the permission of these institutions.

REFERENCES

Abdo, A. A., Ackermann, M., Arimoto, M., et al. 2009, Science, 323, 1688
Ajello, M., Arimoto, M., Axelsson, M., et al. 2019, ApJ, 878, 52
Akerlof, C. W., & Swan, H. F. 2007, ApJ, 671, 1868
Astropy Collaboration, Robitaille, T. P., Tollerud, E. J., et al. 2013, A&A, 558, A33
Astropy Collaboration, Price-Whelan, A. M., Sipőcz, B. M., et al. 2018, AJ, 156, 123
Atwood, W. B., Abdo, A. A., Ackermann, M., et al. 2009, ApJ, 697, 1071
Barthelmy, S. D., Barbier, L. M., Cummings, J. R., et al. 2005, Space Science Reviews, 120, 143
Bloom, J. S., Frail, D. A., & Sari, R. 2001, AJ, 121, 2879
Brasseur, C. E., Phillip, C., Fleming, S. W., Mullally, S. E., & White, R. L. 2019, Astrocut: Tools for creating cutouts of TESS images, , , ascl:1905.007
Corre, D., Buat, V., Basa, S., et al. 2018, A&A, 617, A141
de Ugarte Postigo, A., Thöne, C. C., Bensch, K., et al. 2018, A&A, 620, A190
Del Vecchio, R., Dainotti, M. G., & Ostrowski, M. 2016, ApJ, 828, 36
Evans, P. A., Willingale, R., Osborne, J. P., et al. 2010, A&A, 519, A102
Fruchter, A., Krolik, J. H., & Rhoads, J. E. 2001, ApJ, 563, 597
Gaia Collaboration, Brown, A. G. A., Vallenari, A., et al. 2018, A&A, 616, A1
Gehrels, N., Chincarini, G., Giommi, P., et al. 2004, ApJ, 611, 1005
Ghirlanda, G., Nava, L., Ghisellini, G., Celotti, A., & Firmani, C. 2009, A&A, 496, 585
Ghirlanda, G., Nappo, F., Ghisellini, G., et al. 2018, A&A, 609, A112
Goldstein, A., Hamburg, R., Wood, J., et al. 2019, arXiv e-prints, arXiv:1903.12597
Gropp, J. D., Klingler, N. J., Lien, A. Y., et al. 2019, GRB Coordinates Network, 26008, 1
Grupe, D., Gronwall, C., Wang, X.-Y., et al. 2007, ApJ, 662, 443
HI4PI Collaboration, Ben Bekhti, N., Flöer, L., et al. 2016, A&A, 594, A116
Hu, Y. D., Fernandez-Garcia, E., Castro-Tirado, A. J., et al. 2019, GRB Coordinates Network, 26017, 1
Kann, D. A., Klose, S., Zhang, B., et al. 2010, ApJ, 720, 1513
Kim, V., Pozanenko, A., Krugov, M., et al. 2019, GRB Coordinates Network, 26018, 1
Kobayashi, S., Mészáros, P., & Zhang, B. 2004, ApJ, 601, L13
Kostov, V. B., Mullally, S. E., Quintana, E. V., et al. 2019, AJ, 157, 124
Krühler, T., Greiner, J., Afonso, P., et al. 2009, A&A, 508, 593
Krühler, T., Schady, P., Greiner, J., et al. 2011, A&A, 526, A153
Li, L., Wang, Y., Shao, L., et al. 2018, ApJS, 234, 26
Lightkurve Collaboration, Cardoso, J. V. d. M., Hedges, C., et al. 2018, Lightkurve: Kepler and TESS time series analysis in Python, Astrophysics Source Code Library, , , ascl:1812.013
Madau, P. 1995, ApJ, 441, 18
Madau, P., & Rees, M. J. 2000, ApJ, 542, L69
Margutti, R., Genet, F., Granot, J., et al. 2010, MNRAS, 402, 46
Marshall, F. E., Antonelli, L. A., Burrows, D. N., et al. 2011, ApJ, 727, 132
Meegan, C., Lichti, G., Bhat, P. N., et al. 2009, ApJ, 702, 791
Molinari, E., Vergani, S. D., Malesani, D., et al. 2007, A&A, 469, L13
Nelder, J. A., & Mead, R. 1965, Computer Journal, 7, 308
Oates, S. R., Page, M. J., Schady, P., et al. 2009, MNRAS, 395, 490
Pei, Y. C. 1992, ApJ, 395, 130
Ricker, G. R., Winn, J. N., Vanderspek, R., et al. 2015, Journal of Astronomical Telescopes, Instruments, and Systems, 1, 014003
Roming, P. W. A., Koch, T. S., Oates, S. R., et al. 2017, ApJS, 228, 13
Sari, R., & Piran, T. 1999, ApJ, 520, 641
Sari, R., Piran, T., & Narayan, R. 1998, ApJ, 497, L17
Schady, P., & Bolmer, J. 2019, GRB Coordinates Network, 26176, 1
Smith, K. L. 2019, Astronomische Nachrichten, 340, 308
Stassun, K. G., Oelkers, R. J., Pepper, J., et al. 2018, AJ, 156, 102
Toma, S., Niwano, M., Adachi, R., et al. 2019, GRB Coordinates Network, 26019, 1
Totani, T., Kawai, N., Kosugi, G., et al. 2006, PASJ, 58, 485
Wang, X.-G., Liang, E.-W., Li, L., et al. 2013, ApJ, 774, 132
Watson, A. M., Butler, N., Becerra, R. L., et al. 2019a, GRB Coordinates Network, 26010, 1
Watson, A. M., Butler, N., Kutyrev, A., et al. 2019b, GRB Coordinates Network, 26015, 1
Zheng, W., Filippenko, A. V., & KAIT GRB Team. 2019, GRB Coordinates Network, 26011, 1